fluids

MDPI

Article

Numerical Analysis of the Primary Gas Boundary Layer Flow Structure in Laser Fusion Cutting in Context to the Striation Characteristics of Cut Edges

Madlen Borkmann * and Achim Mahrle

Fraunhofer-Institut für Werkstoff und Strahltechnik IWS, D-01277 Dresden, Germany;
achim.mahrle@iws.fraunhofer.de
* Correspondence: madlen.borkmann@iws.fraunhofer.de

Abstract: In cutting metals with solid-state lasers, a characteristic cutting edge structure is generated whose formation mechanisms still elude a consistent explanation. Several studies suggest a major contribution of the pressurized gas flow. Particular emphasis must be devoted to the gas boundary layer and its developing flow characteristics, since they determine the heat and momentum exchange between the cutting gas and the highly heated melt surface and thus the expulsion of the molten material from the kerf. The present study applies a CFD simulation model to analyze the gas flow during laser cutting with appropriate boundary conditions. Specifically, the gas boundary layer development is considered with a high spatial discretization of this zone in combination with a transition turbulence model. The results of the calculation reveal for the first time that the boundary layer is characterized by a quasi-stationary vortex structure composed of nearly horizontal geometry- and shock-induced separation zones and vertical vortices, which contribute to the transition to turbulent flow. Comparison of the results with the striation structure of experimental cut edges reveals a high agreement of the location, orientation, and size of the characteristic vortices with particular features of the striation structure of cut edges.

Keywords: laser fusion cutting; supersonic gas flow; simulation model; boundary layer development; boundary layer transition; gas flow separation; shock wave boundary layer interaction; momentum and heat transfer

Citation: Borkmann, M.; Mahrle, A. Numerical Analysis of the Primary Gas Boundary Layer Flow Structure in Laser Fusion Cutting in Context to the Striation Characteristics of Cut Edges. *Fluids* **2022**, *7*, 17. https://doi.org/10.3390/fluids7010017

Academic Editor: Yufeng Yao

Received: 25 November 2021
Accepted: 24 December 2021
Published: 31 December 2021

1. Introduction

Laser fusion cutting is an advanced manufacturing process for the non-contact separation of diverse metals and non-metals in a wide range of thicknesses. During the process, a laser beam is guided along a contour, partially absorbed at the material surface and, as a result, the material is melted locally. In addition, a high-pressure gas jet is usually guided coaxially to the laser beam, which expels the melt produced from the resulting kerf (Figure 1a). Because of the gas pressure used, usually above 1.0 MPa, the gas flow exceeds the speed of sound in the processing zone. The performance and quality criteria for the cutting of high-alloy corrosion-resistant steels considered here include the achievable cutting speed, the gap geometry with a desired perpendicularity of the edges, their roughness, and the melt adhesion on the underside of the material. The process principle and the process-determining influencing variables are described in detail in the basic literature [1–3].

Open questions remain on the formation mechanisms for the characteristic structure of the cut edges and on burr formation on the underside. A clarification of the mechanisms is not only interesting from the point of view of basic research but is also highly relevant for the industrial applications of laser cutting, since the characteristics mentioned are decisive for the quality. Since the market introduction of fiber and disk lasers (wavelength of approximately 1 μm) in the high-power range, it has become clear that the process result is strongly dependent on the laser wavelength used, compared to the CO_2 laser (wavelength of 10.6 µm) previously available [4–7]. The advantages of fiber and disk lasers in the area of process performance could be justified very well via the wavelength dependence of the angle-dependent absorption [8,9]. In contrast, the generation of striations with higher roughness of the cutting edge and the susceptibility to burr formation occurring with fiber and disk lasers still awaits a consistent and generally accepted explanation.

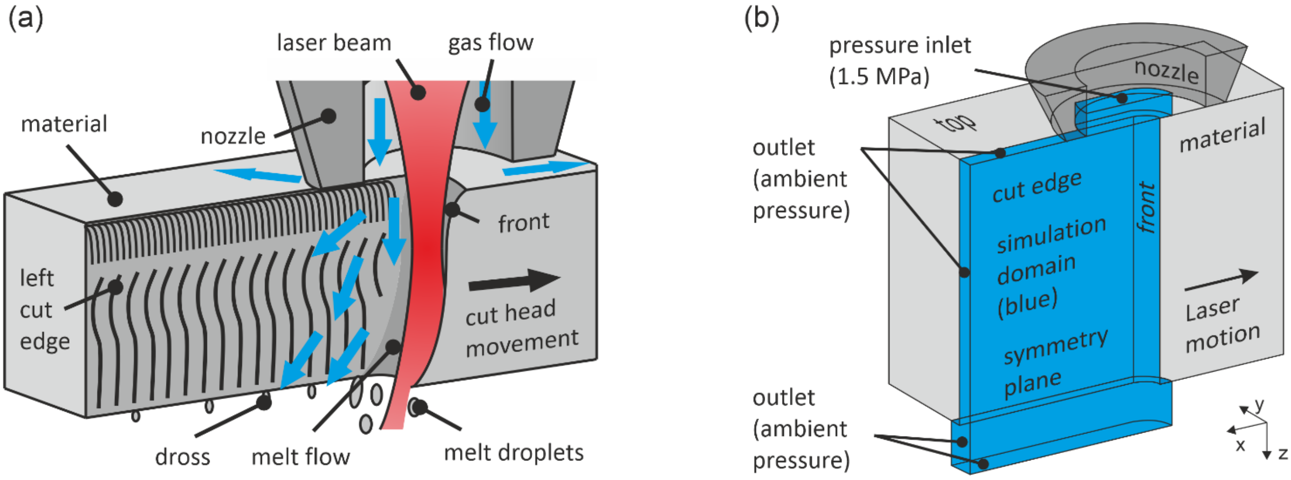

Figure 1. (**a**) Scheme of laser fusion cutting; (**b**) Geometric model and applied boundary conditions, simulation domain for the gas flow highlighted in blue.

One challenge in developing a comprehensive understanding of the process is the difficulty of directly observing the physical processes taking place in the interaction zone between the laser beam and the material. To investigate the flow behavior of the melt under near-process conditions, the trim-cut technique was developed, in which the laser beam is guided along the material edge and the second cut edge is replaced by a transparent glass plate [10]. The method has been used by various research groups to visualize melt flow and striation formation [11–14]. It was found that the trim-cut method reflects the structure formation at the top edge but certainly the changed gas flow modifies the further results. The process boundary conditions were modified by Hirano and Fabbro so that the upper kerf area could be investigated by means of high speed imaging [15]. They were able to show that the melt flow splits into a near-frontal flow and a lateral flow along the edge, and that the latter finally determines the formation of the striations in the area under consideration. Recently, Lind et al. investigated the process behavior by X-rays and were able to verify melt flow along the edges for the subsequent kerf, which has a significant effect on the resulting kerf shape and whole striation formation [16]. The latest results of Lind et al. [17], generated by synchrotron X-ray, even resolved the melt film directly in the cutting process. Sawannia et al. [18] inspected the cutting front during processing by a goniometer and reported moving melt structures along the entire front with the corresponding velocities. However, the cause of the observed melt flow cannot be determined solely on the basis of the diverse process visualizations.

Nevertheless, the understanding of striation formation is considered a primary key to capturing the involved dynamic phenomena in laser cutting [19]. Already for cutting with CO_2 lasers three different types of striations along the edge have been described [20–22]. This differentiation no longer seems sufficient for cutting with solid-state lasers, and recently at least five zones have been identified on cut edges in 10 mm thick stainless steel [23]. Interestingly, the high-resolution microscope images of the cut edges also show accumulations of melt with a spiral surface structure in the spatial context of striations, suggesting the contribution of gas flow as the cause of formation of the overall structure. In addition, a correlation analysis between the experimentally measured roughnesses of the cut edges with the numerically determined shear stress distributions was found [24]. The study links the simulation of the gas flow with the experimental results by implementing experimentally determined realistic interface geometries in the calculation. Interestingly, the backward shear stresses in the kerf correlate with the measured roughnesses. Thus, both structural details and correlations between roughness and gas simulation indicate the significance of gas flow in the formation of edge structure but are not adequately accounted for in existing modeling approaches to laser fusion cutting.

The basic flow characteristics of the gas during laser cutting has already been extensively studied, as it is considered to be of great importance for the process performance. In the first comprehensive characterizations, a direct correlation between gas pressure and achievable cutting speed was found for cutting with CO_2 lasers [25,26]. In another fundamental work by Petring et al., the gas flow in transparent kerf models was studied by means of schlieren analysis, and the interaction of shock structure and gas boundary layer was pointed out for the first time [27]. Since then, numerous studies on cutting gas characteristics and nozzle designs and arrangements have been published with a recent review by Riveiro et al. [28]. In addition to experimental investigations, simulation using CFD is playing an increasingly important role [5,29–34]. For the characteristics of the global flow, very good agreement is achieved with experimental visualizations using schlieren analysis, owing to the well-describable state behavior of the gases and efficient turbulence models. However, the CFD analyses to the present, as well as the schlieren analyses, only reveal the macrostructure of the flow field. The direct interaction region for energy and momentum transfer between gas flow and melt film surface, the gas boundary layer, has not yet been investigated under near-process conditions. Thus, it is not surprising that possibly vital links between cut edge structure and gas flow characteristics could not detected until now. Recently, the boundary layer development and heat and momentum transfer for laser fusion cutting were for the first time analyzed by Borkmann et al. using analytical considerations of boundary layer theory and thermofluid dynamics [35]. They showed that for realistic boundary conditions (i) the experimentally determined striation structures occur within the boundary layer thickness, and that (ii) a boundary layer in the transition regime between laminar and turbulent at the entire cut edge and (iii) not a fully run-in turbulent boundary layer flow, which would justify simplifying assumptions regarding pressure and shear effects of the gas as in [36], must be assumed. In addition, the locally strongly varying heat and momentum transfer of a lengthy transitional boundary layer with manifestation especially of the stationary instability modes in the solidifying melt film was presumed. Motivated by these results, the present work investigates the boundary layer development in laser cutting by CFD with boundary layer resolution and considers the necessary boundary conditions for pressure and wall temperature and the temperature-dependent material properties.

2. Materials and Methods

The simulation of the cutting gas flow was performed by use of the commercial fluid dynamics code ANSYS FLUENT 18.1. The underlying model was based on the Reynolds-averaged Navier–Stokes equations (RANS) for compressible fluids. The equation system consisted of the conservation of mass, momentum, and energy and the equation of state for ideal gases [37]. The equation of conservation of mass is as follows:

$$\frac{\partial \rho}{\partial t} + \frac{\partial}{\partial x_i}(\rho u_i) = 0, \tag{1}$$

and the ensemble-averaged momentum equations in tensor-notation are

$$\frac{\partial}{\partial t}(\rho u_i) + \frac{\partial}{\partial x_j}(\rho u_i u_j) = -\frac{\partial p}{\partial x_i} + \frac{\partial}{\partial x_j}\left[\eta\left(\frac{\partial u_i}{\partial x_j} + \frac{\partial u_j}{\partial x_i} + \frac{2}{3}\delta_{ij}\frac{\partial u_l}{\partial x_l}\right)\right] + \frac{\partial}{\partial x_j}\left(-\rho\overline{u'_i u'_j}\right). \tag{2}$$

The energy equation solved in ANSYS FLUENT has the following form [34]:

$$\frac{\partial}{\partial t}(\rho E) + \nabla \cdot \left(\vec{v}(\rho E + p) \right) = \nabla \cdot \left(k_{eff} \nabla T + \bar{\bar{\tau}}_{eff} \cdot \vec{v} \right) \tag{3}$$

where k_{eff} is the effective thermal conductivity. The equation of state for ideal gases is

$$p = \rho \, R_S \, T, \tag{4}$$

with $R_{S,N_2} = 286.8$ J/kg K the specific gas constant of nitrogen.

The turbulence modeling of the quasi-steady core flow was carried out by the SST k-ω turbulence model and the unknown Reynolds stress tensor was modeled by the mean velocity gradients via the Boussinesq hypothesis:

$$-\rho \overline{u'_i u'_j} = \eta_t \left(\frac{\partial u_i}{\partial x_j} + \frac{\partial u_j}{\partial x_i} \right) - \frac{2}{3} \left(\rho k + \eta_t \frac{\partial u_k}{\partial x_k} \right) \delta_{ij}, \tag{5}$$

with the turbulent viscosity η_t and the turbulence kinetic energy k. In the applied turbulence model, an additional transport equation was solved for each of the turbulence kinetic energy k and the specific dissipation rate ω. The precise formulation of the production, diffusion, and dissipation terms can be found in [37]. The turbulent viscosity was evaluated as a function of k and ω. To account for the development of the gas boundary layer from laminar to turbulent the Intermittency transition model extension was used. A variable intermittency was applied that specifies the rate of transition of the boundary layer from laminar to turbulent. For the intermittency an additional transport equation was solved [37]. For intermittency equal to zero the transition model extension dampened the turbulence model and quasi-laminar Navier–Stokes equations were solved in the associated area. In regions with intermittency equal to one a fully turbulent flow was calculated based on the applied turbulence model. This resulted in a more accurate calculation of boundary layer development, wall near-flow structure and derived quantities, e.g., momentum and heat transfer at the walls [38,39]. Therefore, the modeling approach was focused on the simulation of the development of the boundary layer. A great advantage of the method is that the computational effort for calculating the quasi-static basic flow is minimized compared to scale-resolving methods, e.g., Large Eddy Simulations. The transition model is validated for a wide range of turbo-machinery and aeronautical test cases [39].

The current study focused on the gas flow in laser fusion cutting of stainless steel of medium material thicknesses (>6 mm). Accordingly, in the first approach assumptions for the simulation of the cutting gas flow were made:

- In case of cutting thicker material (>6 mm) with high brightness fiber lasers the slope of the cutting front is typically >86°, as stated in [8], and therefore is negligible for the gas flow.
- The front of the cut kerf is estimated as semi-cylinder whose axis coincides with the axis of the conical and circular nozzle, since mostly circular laser intensity distributions are used.
- For the cut kerf, parallel walls, and a constant kerf diameter of 800 µm are assumed in first approximation since kerf width is very small in comparison to the material thickness and the kerf ratio (width at top side to width at bottom side) is close to 1 [40].
- The walls are modeled as solid without a moving melt film. Since the velocity scale of the gas flow is two magnitudes higher than for the melt flow, it can be assumed that the friction forces exerted on the solid walls are comparable to those on the moving liquid melt film [18].
- The cutting gas jet is usually guided coaxially and symmetrically to the laser beam and for cuts of good quality, the opposite cut edges are the very same. Therefore, a symmetry plane along the feed direction is applied.

- The effect of the laser radiation absorption at front and kerf is approximated as temperature boundary condition at front and kerf walls. Magnitude and extension are derived from experimental results in [41].
- The commonly used cutting gas nitrogen is modeled according to the ideal gas equation of state with realistic inlet boundary conditions for pressure (1.5 MPa) and temperature [40].
- Typically, nozzle stand-off, i.e., the distance between nozzle outlet and sheet surface, of less than 1 mm is used when cutting thick sheet metal [40]. With the nozzle diameter being a multiple thereof, the main acceleration of the gas takes place within the kerf and the pressure at the top coincides with the gas pressure at the inlet. Therefore, a directly attached nozzle with a zero nozzle stand-off is assumed. The comparability of the flow conditions in the process zone was confirmed in preliminary studies.

The geometric model and the boundary conditions are depicted in Figure 1b. At the inlet within the nozzle a total pressure of 1.5 MPa and a total temperature of 300 K were applied. A fully turbulent flow with an intermittency of 1 and a turbulent intensity Tu = 0.1% was used. The results of a variation study in Appendix A showed that the specific choice of turbulent intensity in this case had little effect on the simulation result.

At the pressure outlets at the top of the kerf, the back side, and underneath the material ambient pressure and temperature were applied. In case of supersonic outflow, this fixed boundary condition was substituted automatically, and the supersonic flow conditions were extrapolated to the boundary. This was necessary because of the information flow in supersonic flows, which is restricted to the downstream direction. With the supersonic outflow condition, the area underneath the material was restricted to a small volume of 1 mm thickness. Additionally, backflow at ambient conditions was allowed at the outlets, which can result in the suction of ambient atmosphere into the simulation domain at the top and backside of the kerf and underneath the material.

The walls of the nozzle, top of material, front, kerf edges, and bottom material were defined as stationary with a no-slip shear condition. They were assumed to be aerodynamically smooth and, particularly for the kerf edge, the influence of the cut edge roughness of typically about 50 µm R_Z was disregarded in the first instance. At front and kerf edges, a smoothed temperature distribution approximated from experimental results [41] was applied. It was reasonable to assume that a wall temperature ranging between the melting and vaporization temperatures of stainless steel was present in the process zone owing to the liquid melt film. Accordingly, at the front and forepart of the kerf edge, a constant temperature of 2500 K was assumed. Behind the presumed processing zone, the temperature reduced linearly to 353 K within 1 mm from heat conduction to the material and then remained constant. The associated formula is given in Equation (6).

$$T(x,z) = \begin{cases} T_{max} & ; x < x_0 \\ T_{min} + (1 - x/x_0)(T_{max} - T_{min}) & ; x_0 \leq x \leq x_1 \\ T_{min} & ; x > x_1 \end{cases} \tag{6}$$

$$\text{and } x_0 = f(z) = z/z_0 \cdot \Delta x,\ x_1 = x_0 + \Delta x$$

$$z_0 = 6\text{ mm};\ \Delta x = 1\text{ mm};\ T_{max} = 2500\text{ K};\ T_{min} = 353\text{ K}.$$

The correlation between pressure, density, and temperature of the cutting gas nitrogen was modeled according to the equation of state (Equation (4)). In the pressure range examined, the viscosity of nitrogen was primarily dependent on the temperature. This temperature dependency was modeled by Sutherland's law

$$\eta(T) = \eta_0 \left(\frac{T}{T_0}\right)^{\frac{3}{2}} \frac{T_0 + S}{T + S}, \tag{7}$$

with $\eta_0 = 1.663 \times 10^{-5}\ \frac{\mathrm{kg}}{\mathrm{ms}}$, $T_0 = 273.1$ K and $S = 106.67$ K. Thus, the applied boundary conditions and the temperature-dependent material properties matched the conditions specified in [35].

For transition models, an appropriate resolution of the boundary layer is crucial. A mesh resolution normal to the wall of at least $y^+ \leq 1$ is recommended for the non-dimensional distance y^+ for the first grid cell [39]. In this simulation study, a limit value of $y^+ \leq 0.5$ was fulfilled for the cutting gas flow in the entire processing zone. Triangular prism layers were used in the near-wall region with a thickness of 1 µm for the first layer, an expansion ratio of 1.05, and a maximal number of 30 layers. The core flow region was meshed with tetrahedrons and converted to polyhedrons. The resulting mesh consisted of 36.3 million nodes and 12.2 million cells, and the surface mesh is shown in Figure 2. Preliminary simulation experiments with a coarser resolution of the boundary layer, coarser than the recommended $y^+ \leq 1$, significantly differed in some parts from the results obtained here, e.g., in separation and recirculation zones.

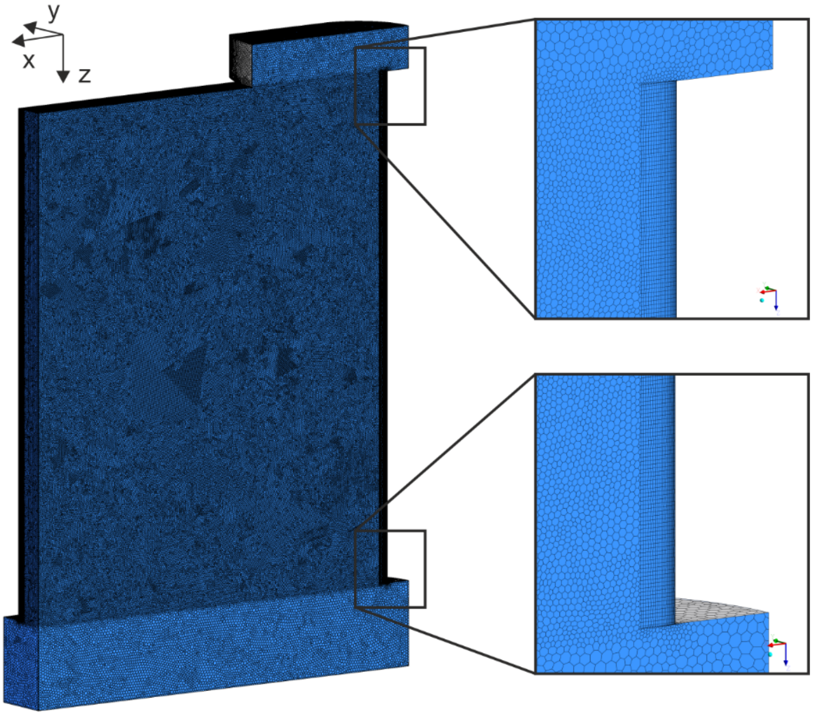

Figure 2. Surface mesh and detailed views of the prism layers at front top and bottom corner.

For initialization a built-in hybrid initialization method with default settings was executed [37]. For initialization of velocity and pressure the Laplace equation was solved. All other variables, such as temperature and turbulence, were interpolated based on the specified boundary conditions. To achieve a stationary solution the pressure-velocity-coupled algorithm was applied, and for all simulation variables a spatial discretization of the second order was used. The solution required approximately 300 iterations for a convergence of at least three orders of magnitude (residual convergence plot in Figure A2, Appendix B).

3. Results

The gas flow was accelerated in the nozzle and reached sonic speed at the smallest flow cross-section near the kerf top because of the pressure ratio between inlet and ambient conditions. Afterwards, within the cut kerf, the gas flow was further accelerated to supersonic velocity. This region in the kerf was characterized by a complex shock structure, which was not only determined by the geometry of the kerf but also by local flow features.

3.1. Flow Structure

In Figure 3 distributions of velocity magnitude at the symmetry plane and a kerf cross-cut at beam axis are depicted. At the kerf entrance the gas flow was slightly below sonic speed. At the upper edge a geometry-induced separation of the flow occurred because of the deflection of the flow. This separation was found at the kerf sides (Figure 3a (1)) and front (Figure 3b) underneath the nozzle.

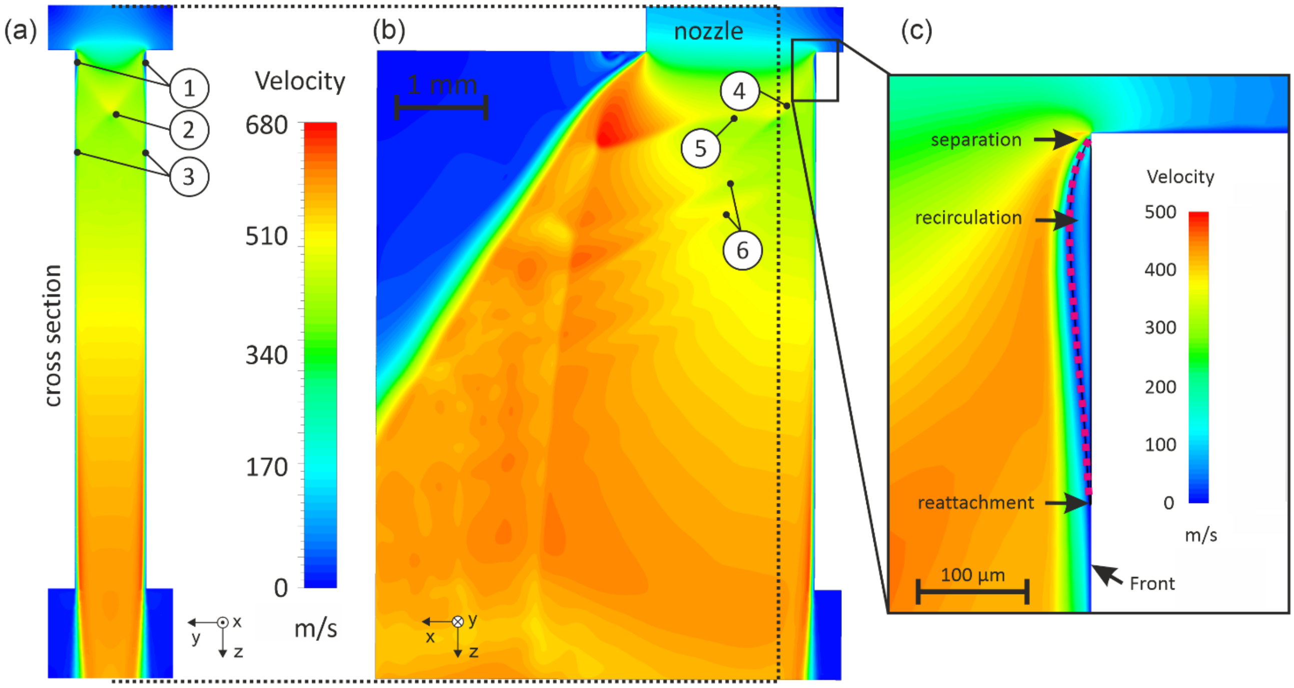

Figure 3. Distributions of velocity magnitude. (**a**) At the cross-section at the beam/nozzle axis; (**b**) at the symmetry plane. (**c**) Enlarged view of the separation, recirculation, and reattachment at the top front corner. Because of the regular kerf shape, the front separation almost coincides with the separation on the top kerf edge corner in (**a**).

In Figure 3c a detailed view of the separation is shown. The red-dotted line divides the recirculation zone (with flow direction to the top) from the main flow, and the recirculation reached a velocity of up to 100 m/s. The length of the separation from separation point to reattachment was about 340 µm, which was almost constant along the upper edge, and a width of 40 µm. Coincident to the separation the flow reached sonic speed and the flow deflection from reattachment resulted in the formation of a so-called reattachment shock. This 3D reattachment shock emanating from the gas flow separation at the upper corner was the origin of a complex shock structure in the kerf. In the middle of the kerf the shocks emanating from front (4) and opposing sides interacted elaborately. Near the axis of the front cylinder, where shock waves of the entire front area converged, an irregular shock–shock interaction with the formation of a Mach stem was found (2). In contrast, for the sole interaction of the side shocks in the rear part of the kerf a regular shock–shock interaction was formed (5). Afterwards, the shocks interacted with the gas boundary layer at the kerf sides and caused local separations with recirculation from the associated pressure rise (3). At these separations the incident shocks were each split into two weaker shocks, one at separation and one at reattachment. As a result, multiple shock–shock interactions (6) and subsequent shock–boundary-layer interactions occurred downstream.

Within the chosen modeling approach, the intermittency was of special importance as a control variable of the local flow mode. In the calculation, the core flow was treated as turbulent throughout. The thickness of the fluid dynamic boundary layer, where the velocity changed from zero at the wall to the velocity of the core flow, was between 50 and 80 µm over the entire running length at front and edge. This was due to boundary layer thickening as a result of inflow separation and subsequent gas acceleration. In contrast, the boundary layer part in the upper kerf, which was characterized as laminar by intermittency, was only a fraction of about 10 µm of the total boundary layer. Downstream, the laminar fraction of the boundary layer increased continuously until the entire fluid dynamic boundary layer was detected as laminar at the lower edge. Furthermore, it was observed that the thermal boundary layer, within which the gas temperature changed from the wall temperature to the core flow temperature, correlated with the laminar boundary layer fraction. From this, a relaminarization effect of the growing temperature boundary layer owing to the increase in viscosity was concluded. Disturbances already introduced into the boundary layer were thus only weakly amplified or attenuated. This relaminarization effect came into play particularly in the vicinity of the wall because of the high temperatures and presumably had a significant effect on the interaction of the gas with the surface.

The applied modeling approach allowed not only the evaluation of the boundary layer flow state but also the revealing and characterization of definite vortex structures within the boundary layer through the weakening of the turbulence model. Accordingly, vortex visualizations by the isosurfaces of λ_2 criterion are shown in Figure 4. The presence of vortices was limited to the boundary layer, for the fully turbulent core flow no eddies were found. The color indicates the rotational direction around z-direction, where blue vortices are right-handed (clockwise rotating with view in flow direction) and red ones are left-handed. In this visualization the separation at the top corner can clearly be seen (7) and a striped pattern of counterrotating vertical vortices becomes obvious. The horizontal cross-cut at z = 100 µm (Figure 4c) shows that the counterrotating vortices are located at the outer edge of the separation.

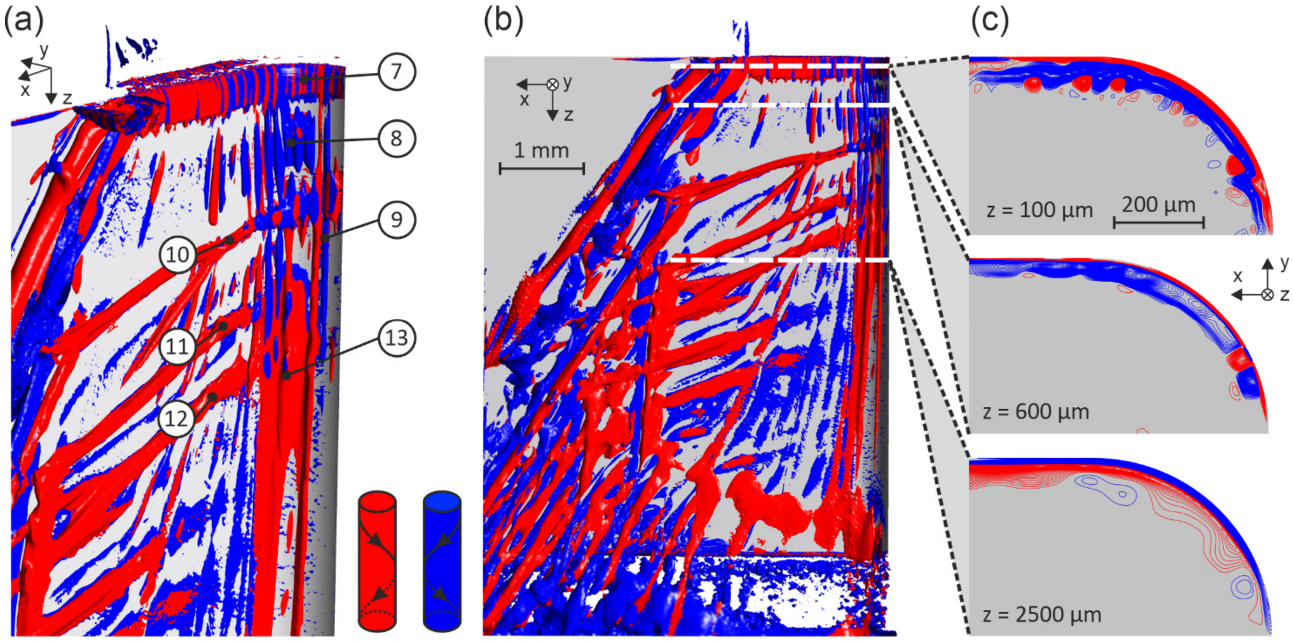

Figure 4. Vortex visualization by means of isosurfaces of λ_2 criterion for $\lambda_2 = -4.89 \times 10^9$ s^{-2}, colored by z-component of vorticity. Blue areas indicate right-handed and red left-handed vortex cores. (**a**) Detailed view of the upper front at an angle from behind. (**b**) Overall view of front and kerf edge. (**c**) Vortex visualization on horizontal cross-sections by means of isolines of the vorticity z-component, viewed downwards in flow direction. Blue isolines indicate vortices rotating in the clockwise direction (dextrorotatory, $\omega_z = 7 \times 10^4$–1×10^7 s^{-1}) and red isolines vortices rotating in the opposite direction (levorotatory, $\omega_z = -7 \times 10^4$–$1 \times 10^7$ s^{-1}).

There are two areas with particularly distinctive vortex pairs, firstly, one pair near the front symmetry and secondly, several pairs laterally at the transition area of front and cut edge. The lateral size of one vortex pair is 80–110 µm. After the reattachment right-handed and vertically aligned vortices dominate the boundary layer and the left-handed vortices become attenuated ((8) and c at z = 600 µm). Only the front vortex pair near the symmetry is retained at least up to the middle of the material (9).

The vortex visualization also shows the separations with recirculation that were induced by the shock–boundary-layer interactions. The first shock–boundary-layer interaction (10) extends over the entire front and side with a particularly massive separation and recirculation at the front due to the strength of the incident shock in this area. For the subsequent shock–boundary-layer interactions with the weaker shocks ((11), (12)) the separations are restricted to the kerf sides and gradually decrease in strength and extent in the downstream direction. Following the first shock–boundary-layer interaction, the right-handed vortices are attenuated, and new left-handed vortices appear near the wall and become amplified ((13) and c at z = 2500 µm). In the downstream direction the vortices become slightly but increasingly bent backward. Additionally, the lateral wavelength of the vortices increases in the downstream direction. At the bottom edge an irregularly shaped separation is formed with locally varying extents. Actually, the modulation seems to be related to the presence and lateral extent of the vertical vortices.

The described vortex structure of the boundary layer is almost steady state, particularly the vertically oriented vortices. Further time-dependent calculations with a time step size of $\Delta t = 2 \times 10^{-8}$ s showed that additionally at least the inflow separation oscillated at a frequency of about 30 kHz owing to vortex shedding and shock oscillation.

3.2. Shear Stress and Heat Flux

The predominant stationary part of the solution resulted in a strong deviation of local wall shear stress and heat flux from the mean values, which are determined by default in standard RANS models assuming a fully turbulent isotropic boundary layer.

Figure 5 shows calculated wall shear lines at front and cut edge determined from the wall shear stress vector and colored by the local wall shear stress magnitude. The wall shear lines indicate the flow direction of a fluid film applied on the wall. Here especially the shock–boundary-layer interactions at the wall are represented by strong local variations of shear stress direction and magnitude. Near the top surface and parallel to it, the reattachment line at the end of the top corner separation is noticeable (14). Within the recirculation zone above the reattachment the shear lines are directed to the upper kerf corner, and thus, a liquid film in this area is driven to the top surface. Potentially, this results in an accumulation of melt within the recirculation area, which in turn affects the characteristics of the separation zone. Downstream of reattachment the shear lines are directed downwards with high shear stresses of up to 4000 Pa at the kerf side. The lateral component of the shear stress is directed to the front symmetry line within the upper part at front and front side and limits the anticipated melt flow to the front area.

The beginning of the first shock–boundary-layer interaction is indicated by a sudden decrease in shear stress magnitude. At the front, the reduction of momentum transfer means a decrease in driving forces on the melt and again can lead to local melt accumulation. It is conceivable that, in association with the oscillation of the shock–boundary-layer interaction, melt waves at the same frequency range were initiated in the separation zone at the front. At the kerf side the lateral component of shear stress becomes dominant, and the shear lines are bent backward in a clearly defined section (15). Consequently, the accumulation of the melt near the front is combined with a localized lateral flow at the kerf side. This results in a redirection of melt from the cut front over the side in a localized rivulet flow.

Downstream of reattachment the shear lines mainly are pointed to the kerf bottom but still exhibit a backward component, which is also followed by the melt flow. Subsequent shock–boundary-layer interactions are restricted to the kerf side and have little influence on the front shear lines (16). Near the plane of symmetry, the shear lines are divided into a ribbon in the center of the front, which remains straight and centralized, and a lateral part, which is slightly but continuously deflected backward. The dividing line (17) coincides with the position of the front vortex pair discussed in Figure 4 (9).

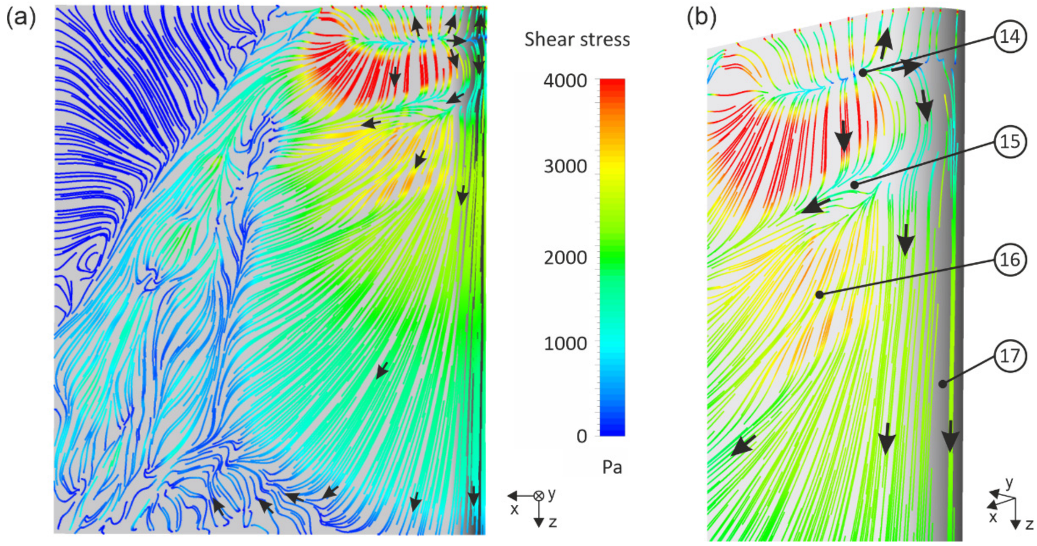

Figure 5. Wall shear lines based on shear stress vector, colored by shear stress magnitude; (**a**) overall view of front and cut edge; (**b**) perspective view of top front and edge.

At the bottom corner the shear stress significantly decreases, although the flow is still attached to the wall and the shear lines are directed downwards at the front area. Behind that, a global separation of the gas flow occurs and the shear lines at the bottom corner are directed upwards. At the separation line the boundary layer finally detaches, and an open recirculation is formed, which sucks ambient atmosphere from underneath the material into the kerf. For an assumed melt film, this means the accumulation of material at the lower edge with reduced removal or, in the rear area, even remaining melt residues in the cut kerf.

The local heat flux density at front and kerf side was mainly influenced by the vertical eddies in the boundary layer (Figure 6). The streaks with high local heat transfer coincide with the location of a counterrotating vortex pair. In a series of counterrotating vortices, the wall-normal velocity component between two vortices is alternately directed once towards the wall and once away from it. If the wall-normal velocity component is directed toward the wall, cooler gas of high momentum is conveyed from the outer edge of the boundary layer directly to the wall. This increases the local gradients of temperature and velocity and hence the heat transfer. In contrast to this, where the hot gas of low momentum is moved away from the wall, the gradients decrease and the heat transfer is reduced compared to the mean values.

Additionally, local boundary layer thickness and pressure influenced the heat transfer. The highest heat flux densities of about 15 W/mm^2 were achieved in the area of the reattachment line of the inflow separation, since the highest pressure and the thinnest boundary layer are reached here (18). Because of the global decrease in pressure and increase in the boundary layer thickness in flow direction, the heat transfer decreased consistently with the shear stresses in the direction of the kerf outlet.

The shock–boundary-layer interactions caused a strong local reduction of the heat transfer on the cut edge (19) owing to the detachment of the boundary layer, recirculation, and heating of the gas over time. For melt accumulating here, this meant a delay in cooling and solidification compared to neighboring regions and a longer interaction with the gas flow in time and space. The strength and the extent of the influence decreased with increasing material thickness, as did the shock strength. In general, the impact of the shock–boundary-layer interactions was limited to the cut sides and the presumed rear edge of the melt film.

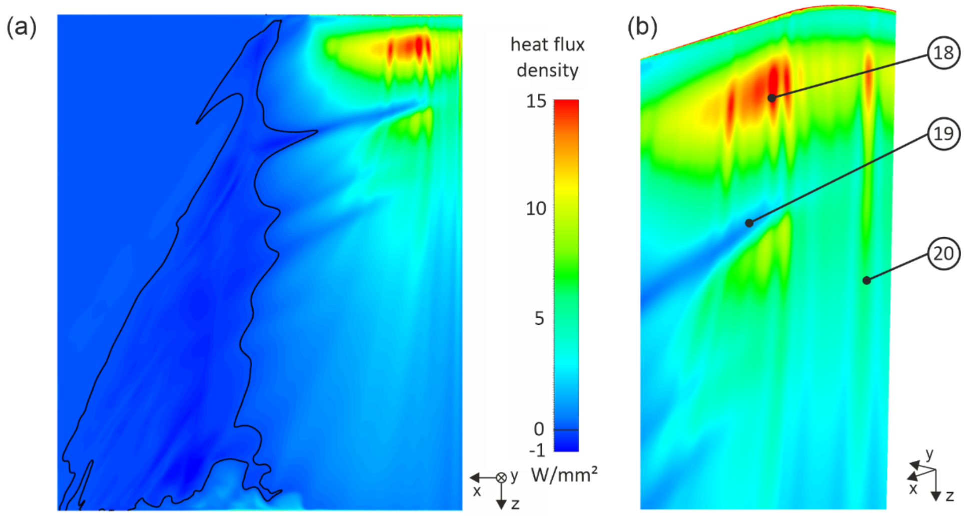

Figure 6. Local heat flux density, zero line marked as shift from cooling the wall by gas flow to heating; (**a**) overall view of front and cut edge; (**b**) perspective view of top front and edge.

In the front area, the front vortex pair is dominant for heat transfer, and its effect can be tracked along the entire front to the bottom edge (20). The simultaneous modulation of the shear stress distribution by the vortex pair divided the front melt film into individual vertical streaks that differ in terms of their temperature, melt film thickness, flow velocity, and thermophysical properties. In a weakened manner, this also applied to all melt film streaks that were separated from an initially homogeneous melt film by additional vortex pairs on the process side.

The calculated total heat flux from the heated front and edge to the cutting gas was 38 W in the simulation area and thus 76 W for the complete processing zone. Compared with the applied laser power of 4 kW, the loss fraction of 1.9% seemed negligible for the energy balance of the process. However, the heat transfer from the wall to the gas had a decisive influence on the flow state of the boundary layer and on the local shear stress distribution and thus the driving force of the melt.

4. Discussion

A fundamental point of discussion was the consistency of the simulation results with the cut edge topography of real laser cutting tests. Figure 7 shows the superposition of the discussed simulation results with a typical cut edge in 6 mm stainless steel (AISI 304) for a YLS 4000 S2T fiber laser with 4 kW. The fiber laser beam with a measured M^2 of 3.58 was focused to a beam waist diameter of 191 µm with a corresponding Rayleigh length of 2.56 mm. A cutting speed of 4.5 m/min was applied. Even at first glance, clear correspondence between the gas dynamics and the cut edge topography becomes apparent. Furthermore, it becomes clear that all three, vortex structure as well as shear stress vector and local heat transfer, influenced the final result. When matching the simulation with the edge, it is also evident that the part in agreement is located near the front at the top of the edge. In flow direction, the area increasingly shifts to the rear on the edge.

In particular, the following similarities can be identified in Figure 7. At the upper edge corner, the extent of the inflow separation coincides with a zone of small striations (21). Likewise, the magnitude of the vortices wavelength is consistent with the observed striations. The reattachment line of the separation matches the abrupt end of the small striations (27). It is presumed that the strong local cooling effect by gas flow (32) resulted in an instant solidification of existing melt residues with clear vortex-structure reproduction. The adjoining zone is characterized by almost no melt residue on the edge. Near the front side, right-handed vortices are dominant (22) and a lateral shear toward the front exists (28). Together with the high shear stresses behind the front (29), this resulted in an effective removal of the melt from the edge in this area.

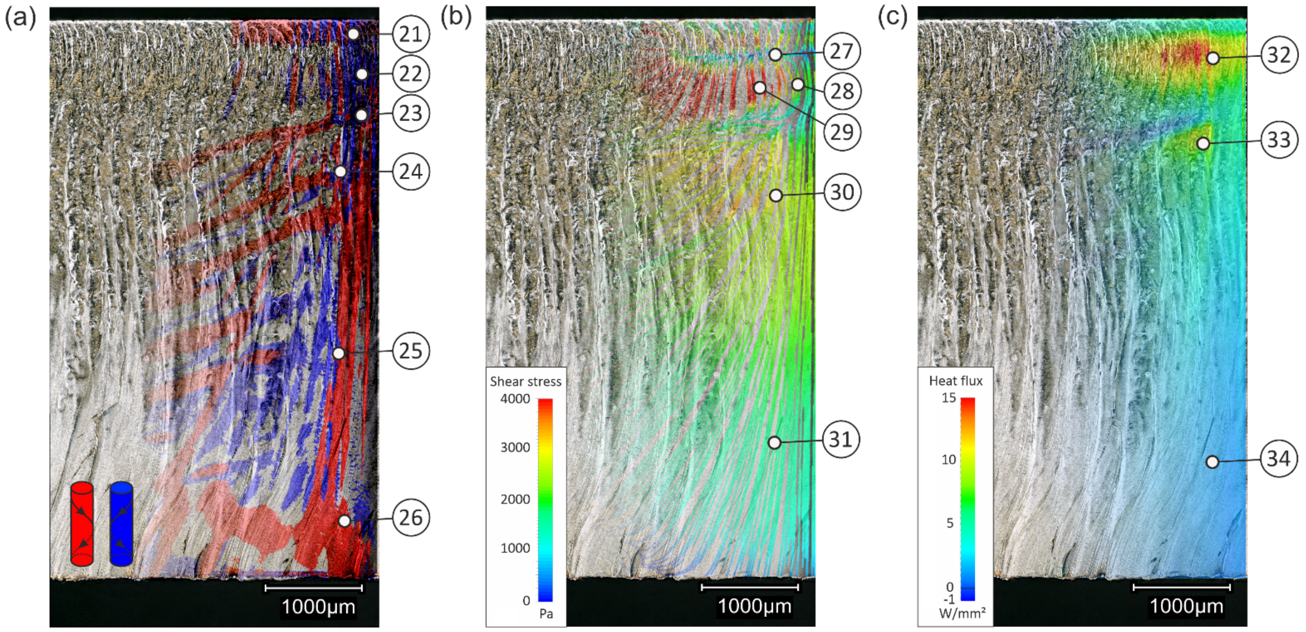

Figure 7. Typical high quality cut edge in 6 mm stainless steel separated by a 4 kW fiber laser at a cutting velocity of 4.5 m/min overlaid with (**a**) boundary layer vortex topography, (**b**) wall shear lines, (**c**) local heat flux density.

For the first shock–boundary-layer interaction, the potential accumulation of melt at the front was already discussed (23). The local lateral shear component and a lower local heat flux can result in a slight lateral melt displacement. In the subsequent zone, the heat transfer locally increased significantly (33), and its geometry agrees well with the structure of the newly starting striations in this zone. Following this, the melt ridges start to show a layer buildup. In the vortex structure a change in dominant rotational direction is found (24) with a slight and constant lateral melt displacement at the front side. At the edge, the sequence of shock–boundary-layer interactions result in wavy wall shear lines (30). Liquid melt in this area also shows a wavy flow pattern in solidification. Accordingly, it can be concluded, that the melt flow was restricted to a front-near area.

In flow direction, the left-handed vortices remain dominant (25) and bend backward just like the striations. At the same time, shear stress (31) and heat transfer (34) were reduced and thus the impulse transferred to the melt, respectively, the velocity and the cooling effect of the gas. A reduction in velocity and cooling resulted in an increase in melt film thickness and temperature and in reduced viscosity and surface tension. The consequential expansion of the melt film across the cut edges with a smoothing of the melt film surface was found in the experimental cut edge structure.

Specifically, the high correlation between simulation and experiment was not evidence of causality and requires further in-depth investigation. However, the confirmation of the predictions compared to the experimental results emphasized the relevance of the gas flow boundary layer to the processing result.

The determined values for boundary layer thickness, shear stress, and heat transfer of this study can be compared to results obtained from empirical correlations of similitude theory [35]. In Figure 8 the respective results at the contact line of front and edge are shown. Because of the complex 3D flow structure, the boundary layer thickness for the simulation was only determined approximately based on the wall-normal z-velocity (Figure 8a). Because of the resolution of the boundary layer separation, the simulation boundary layer thickness deviated significantly from the predicted at the top edge. It was between 50 and 60 μm along the upper half of the processing area and slowly increased to 80 μm up to the bottom edge. The magnitude thus corresponded to a laminar boundary layer of the empirical correlations along most of the edge.

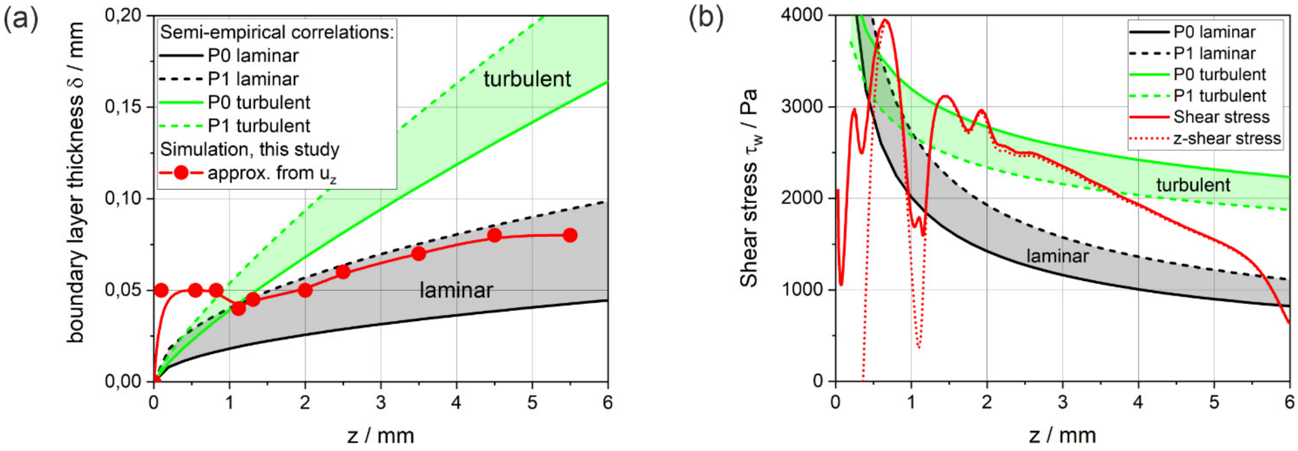

Figure 8. Comparison of results from semi-empirical correlations determined in [35] and simulation results of the current study at the contact line of front and edge for (**a**) boundary layer thickness, (**b**) wall shear stress.

For the local shear stress from simulation, shown in Figure 8b, the strong fluctuations up to a depth of z = 2 mm are apparent. They were the consequence of the separation at the top edge and of the shock–boundary-layer interactions, which were not taken into account in [35]. Nevertheless, the magnitude of the maximum shear stresses agreed well with the estimates of 3000–4000 Pa. In the following part, the simulation results for shear stress highly corresponded to the predicted values for a turbulent boundary layer. In downstream direction the shear stresses of this study were more reduced than suggested by the semi-empirical correlations and thus converged to the laminar reference values. This potential relaminarization has already been observed based on the intermittency and can probably be explained by the influence of the increasing temperature boundary layer on the stability.

Likewise, the heat transfer of 76 W correlated with the predictions of the semi-empirical correlations (24–114 W). Based on the integrated values, however, no conclusions can be drawn about the local flow form of the boundary layer.

The presented results and the comparison to the previous studies suggested that the boundary layer is relatively stable during laser cutting owing to the fact that the pronounced temperature boundary layer and introduced disturbances were only slightly amplified or even attenuated.

5. Conclusions

The results of this study showed that gas dynamics is a crucial aspect of laser cutting that has not received sufficient attention in previous approaches.

Even a low-threshold RANS-simulation model with consideration of transitional boundary layer development is potentially capable of representing the fundamental characteristics of gas flow and gas–material interaction, and a high correlation to experimental cutting results was found.

With this approach, the anisotropic development of the boundary layer can be represented and at least the largest vortex scales of the transition can be reproduced. With the developed model, we expect that it will be possible to identify the causes of various process limitations on the basis of variation calculations with real kerf geometries and temperature distributions, as noticed in [40], and to derive improvements with regard to process parameters, kerf geometry, and laser intensity distribution.

Finally, based on the results presented here, the cutting gas flow may turn out to be a primary key to understanding the formation of striations and the involved dynamic phenomena in laser cutting.

Author Contributions: Conceptualization, M.B. and A.M.; Formal analysis, A.M.; Investigation, M.B.; Methodology, M.B.; Project administration, A.M.; Software, M.B.; Supervision, A.M.; Validation, M.B. and A.M.; Visualization, M.B.; Writing—original draft, M.B.; Writing—review and editing, M.B. and A.M. All authors have read and agreed to the published version of the manuscript.

Funding: This research was funded by the German Research Foundation DFG within the project "Evaluierung dynamischer Lösungsansätze zur Optimierung des Inertgasschneidens von Dickblech mit Laserstrahlquellen hoher Strahlqualität", Contract No. BE1875/36-1. This support is highly appreciated by the authors.

Institutional Review Board Statement: Not applicable.

Informed Consent Statement: Not applicable.

Data Availability Statement: Data sharing is not applicable.

Conflicts of Interest: The authors declare no conflict of interest. The funders had no role in the design of the study; in the collection, analyses, or interpretation of data; in the writing of the manuscript, or in the decision to publish the results.

Appendix A

To our best knowledge, no measurements are available on the turbulent intensity of the gas flow in laser cutting heads. Since the experimental results did not indicate a bypass transition at the upper edge, which is possible for Tu > 1% [36], a turbulent intensity of 0.1% was initially selected. However, in an additional impact study with 1 and 5% turbulent intensity typical for a medium-turbulent flow, we found almost no qualitative or quantitative differences in the simulation results near the processing zone (Figure A1). Differences were only determined at the rear edge of the gas jet and for the flow separation near the bottom edge. Because of the higher turbulent intensity, larger areas of the flow are identified as turbulent here. Therefore, we assume that the turbulent intensity of the core flow has little influence on the boundary layer of the processing zone in this case and, particularly, the geometry-induced separation at the top edge and the thermal boundary conditions determine the development of the boundary layer in laser cutting.

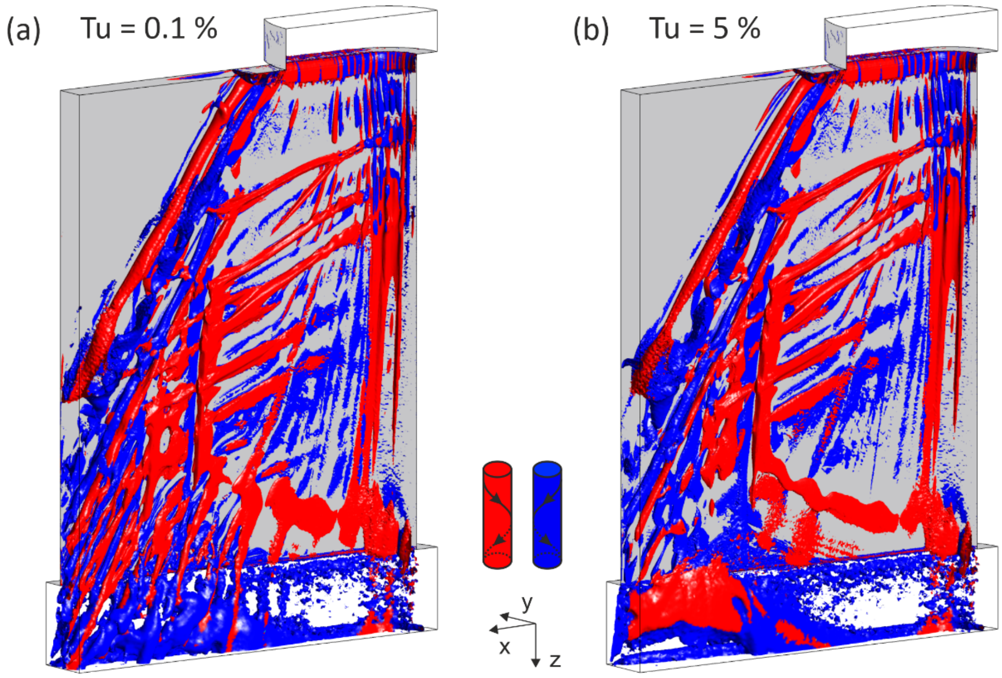

Figure A1. Vortex visualization by means of the isosurfaces of λ_2 criterion for $\lambda_2 = -4.89 \times 10^9$ s^{-2}, colored by z-component of vorticity. Blue areas indicate right-handed and red left-handed vortex cores. (**a**) Tu = 0.1%, (**b**) Tu = 5%.

Appendix B

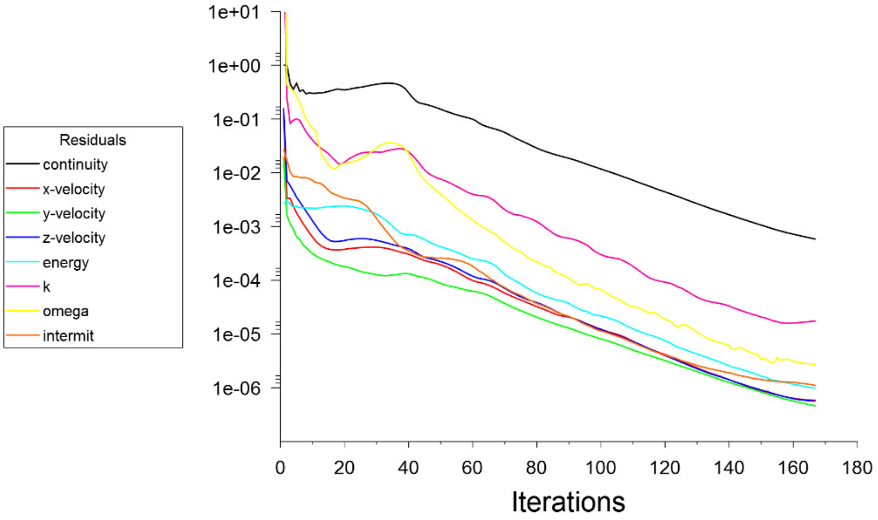

Figure A2. Residue convergence plot.

References

1. Poprawe, R. *Lasertechnik für die Fertigung*; Springer: Berlin/Heidelberg, Germany, 2005; pp. 321–352.
2. Hügel, H.H.; Graf, T. *Laser in der Fertigung*; Vieweg+Teubner: Wiesbaden, Germany, 2009; pp. 174–213.
3. Powell, J.; Petring, D.; Pocorni, J.; Kaplan, A. *LIA Guide to High Power Laser Cutting*, 1st ed.; Laser Institute of America: Orlando, FL, USA, 2017.
4. Wandera, C.; Salminen, A.; Olsen, F.O.; Kujanpäa, V. Cutting of stainless steel with fibre and disk laser. In Proceedings of the 25th International Congress on Applications of Lasers & Electro-Optics, ICALEO 2006, Scottsdale, AZ, USA, 30 October–20 November 2006; pp. 211–220.
5. Sparkes, M.; Gross, M.; Celotto, S.; Zhang, T.; O'Neill, W. Practical and theoretical investigations into inert-gas cutting of 304 stainless steel using a high-brighness laser. *J. Laser Appl.* **2008**, *20*, 59–67. [CrossRef]
6. Scintilla, L.D.; Tricarico, L.; Mahrle, A.; Wetzig, A.; Beyer, E. A comparative study of cut front profiles and absorptivity behavior for disk and CO_2 laser beam inert gas fusion cutting. *J. Laser Appl.* **2012**, *24*, 052006. [CrossRef]
7. Stelzer, S.; Mahrle, A.; Wetzig, A.; Beyer, E. Experimental investigations of fusion cutting stainless steel with fiber and CO_2 laser beams. *Phys. Procedia* **2013**, *41*, 392–397. [CrossRef]
8. Mahrle, A.; Beyer, E. Theoretical aspects of fibre laser cutting. *J. Phys. D Appl. Phys.* **2009**, *42*, 1175507. [CrossRef]
9. Petring, D.; Schneider, F.; Wolf, N.; Goneghany, V.N. The influence of beam quality, power and wavelength on laser cutting and welding. *Laser User* **2009**, *56*, 20–23.
10. Zefferer, H.; Petring, D.; Schulz, W.; Schneider, F.; Herziger, G. Laser beam fusion cutting: Diagnostics and modelling of melt drag and ripple formation. In *Laser in der Technik*; Waidelich, W., Ed.; Springer: Berlin/Heidelberg, Germany, 1994; pp. 574–579.
11. Yudin, P.V.; Petrov, A.P.; Kovalev, O.B. Experimental modeling and high-speed photographic studies of gas laser cutting of sheet metal. In Proceedings of the 27th International Congress on High-Speed Photography and Photonics, Xi'an, China, 17–22 September 2007; Volume 6279.
12. Ermolaev, G.V.; Yudin, P.V.; Briand, F.; Zaitsev, A.V.; Kovalev, O.B. Fundamental study of CO_2 and fibre laser cutting of steel plates with high speed visualization technique. *J. Laser Appl.* **2014**, *26*, 042004. [CrossRef]
13. Arntz, D.; Petring, D.; Jansen, U.; Poprawe, R. Advanced trim-cut technique to visualize melt flow dynamics inside laser cutting kerfs. *J. Laser Appl.* **2017**, *29*, 022213. [CrossRef]
14. Arntz, D.; Petring, D.; Schneider, F.; Poprawe, R. In situ high speed diagnosis—A quantitative analysis of melt flow dynamics inside cutting kerfs during laser fusion cutting with 1 µm wavelength. *J. Laser Appl.* **2019**, *31*, 022206. [CrossRef]
15. Hirano, K.; Fabbro, F. Experimental investigation of hydrodynamics of melt layer during laser cutting of steel. *J. Phys. D Appl. Phys.* **2011**, *44*, 105503. [CrossRef]
16. Lind, J.; Fetzer, F.; Blazquez-Sanchez, D.; Weidensdörfer, J.; Weber, R.; Graf, T. Geometry and absorptance of the cutting fronts during laser beam cutting. *J. Laser Appl.* **2020**, *32*, 032015. [CrossRef]
17. Lind, J.; Fetzer, F.; Hagenlocher, C.; Blazquez-Sanchez, D.; Hummel, M.; Olowinsky, A.; Weber, R.; Graf, T. Influence of the laser cutting front geometry on the striation formation analysed with high-speed synchrotron X-ray imaging. In *IOP Conference Series: Materials Science and Engineering*; IOP Publishing: Bristol, UK, 2021; Volume 1135, p. 012009. [CrossRef]

18. Sawannia, M.; Berger, P.; Weber, R.; Graf, T. Determination of the geometry of laser-cutting fronts with high spatial and temporal resolution. In *IOP Conference Series: Materials Science and Engineering*; IOP Publishing: Bristol, UK, 2021; Volume 1135, p. 012013. [CrossRef]
19. Schulz, W.; Kostrykin, V.; Nießen, M.; Michel, J.; Petring, D.; Kreutz, E.W.; Poprawe, R. Dynamics of ripple formaltion and melt flow in laser beam cutting. *J. Phys. D Appl. Phys.* **1999**, *32*, 1219–1228. [CrossRef]
20. Schuöcker, D. Dynamic phenomena in laser cutting and cut quality. *J. Appl. Phys. B* **1986**, *40*, 9–14. [CrossRef]
21. Zefferer, H. *Dynamik des Schmelzschneidens mit Laserstrahlung*; Shaker-Verlag: Herzogenrath, Germany, 1998.
22. Poprawe, R. Modeling, monitoring and control in high quality laser cutting. *CIRP Ann. Manuf. Technol.* **2001**, *50*, 137–140. [CrossRef]
23. Borkmann, M.; Mahrle, A.; Beyer, E.; Leyens, C. Cut edge structures and gas boundary layer characteristics in laser beam fusion cutting. In Proceedings of the Lasers in Manufacturing Conference, LIM 2019, Munich, Germany, 24–27 June 2019.
24. Borkmann, M.; Mahrle, A.; Beyer, E. Study of correlation between edge roughness and gas flow characteristics in laser beam fusion cutting. In Proceedings of the 10th Conference on Photonic Technologies, LANE 2018, Fürth, Germany, 3–6 September 2018.
25. Fieret, J.; Terry, M.J.; Ward, B.A. Aerodynamic interactions during laser cutting. In *Laser Processing: Fundamentals, Applications, and Systems Engineering*; International Society for Optics and Photonics: Bellingham, WA, USA, 1986; Volume 0668, pp. 53–62.
26. Fieret, J.; Terry, M.J.; Ward, B.A. *Overview of Flow dDynamics in Gas-Assisted Laser Cutting*; SPIE: Bellingham, WA, USA, 1987; Volume 0801, pp. 243–250.
27. Petring, D.; Abels, P.; Beyer, E.; Herziger, G. Werkstoffbearbeitung mit Laserstrahlung, Teil 10: Schneiden von metallischen Werkstoffen mit CO_2-Hochleistungslasern. *Feinw. Messtech.* **1988**, *96*, 364–372.
28. Riveiro, A.; Quintero, F.; Boutinguiza, M.; del Val, J.; Comesana, R.; Lusquinos, F.; Pou, J. Laser cutting: A review on the influence of assist gas. *Materials* **2019**, *12*, 157. [CrossRef]
29. Horisawa, H.; Fushimi, T.; Takasaki, T.; Yamaguchi, S. Impinging jet characterization in a laser cut kerf. In *High-Power Lasers in Manufacturing*; International Society for Optics and Photonics: Bellingham, WA, USA, 2000; Volume 3888, pp. 644–653.
30. Chen, K.; Yao, Y.L.; Modi, V. Gas jet—Workpiece interactions in laser machining. *J. Manuf. Sci. Eng.* **2000**, *122*, 429–438. [CrossRef]
31. Chen, K.; Yao, Y.L.; Modi, V. Gas dynamic effects on laser cut quality. *J. Manuf. Processes* **2001**, *3*, 38–49. [CrossRef]
32. Jun, H.; Guo, S.; Lei, L.; Yan, Z. Characteristic analysis of supersonic impinging jet in laser machining. *Int. J. Adv. Manuf. Technol.* **2008**, *39*, 716–724. [CrossRef]
33. Guo, S.; Jun, H.; Lei, L.; Yao, Z. Numerical analysis of supersonic gas-dynamic characteristics in laser cutting. *Opt. Lasers Eng.* **2009**, *47*, 103–110. [CrossRef]
34. Tamsaout, T.; Amara, E. Numerical simulation of assisting gas flow for laser cutting processes. In Proceedings of the Photonics and Optoelectronics Meetings POEM, Wuhan, China, 2–5 November 2011.
35. Borkmann, M.; Mahrle, A.; Beyer, E.; Leyens, C. Laser fusion cutting: Evaluation of gas boundary layer flow state, momentum and heat transfer. *Mater. Res. Express* **2021**, *8*, 036513. [CrossRef]
36. Halm, U.; Nießen, M.; Schulz, W. Simulation of melt film dynamics in laser fusion cutting using a boundary layer approximation. *Int. J. Heat Mass Transf.* **2021**, *168*, 120837. [CrossRef]
37. *ANSYS Fluent Theory Guide. Release 18.1*; ANSYS, Inc.: Southpointe, Canonsburg, 2017.
38. Menter, F.R.; Langtry, R.B.; Likki, S.R.; Suzen, Y.B.; Huang, P.G.; Völker, S. A Correlation-Based Transition Model Using Local Variables—Part I. *J. Turbomach.* **2006**, *128*, 413–422. [CrossRef]
39. Gerasimov, A. *Guidelines for Setting up Laminar-Turbulent Transition Cases in ANSYS CFD*; ANSYS Guidelines Version 2.0; ANSYS UK Ltd.: Sheffield, UK, 2014.
40. Mahrle, A.; Borkmann, M.; Pfohl, P. Factorial analysis of fibre laser fusion cutting of AISI 304 stainless steel: Evaluation of effects on process performance, kerf geometry and cut edge roughness. *Materials* **2021**, *14*, 2669. [CrossRef]
41. Onuseit, V.; Ahmed, M.A.; Weber, R.; Graf, T. Space-resolved spectrometric measurements of the cutting front. *Phys. Procedia* **2011**, *12*, 584–590. [CrossRef]